# Computationally Efficient Algorithms for Sparse, Dynamic Solutions to the EEG Source Localization Problem

Elvira Pirondini, Behtash Babadi, Gabriel Obregon-Henao, Camilo Lamus, Wasim Q. Malik, Matti S. Hämäläinen, and Patrick L. Purdon

***Abstract*—*Objective*: Electroencephalography (EEG) and magnetoencephalography noninvasively record scalp electromagnetic fields generated by cerebral currents, revealing millisecond-level brain dynamics useful for neuroscience and clinical applications. Estimating the currents that generate these fields, i.e., source localization, is an ill-conditioned inverse problem. Solutions to this problem have focused on spatial continuity constraints, dynamic modeling, or sparsity constraints. The combination of these key ideas could offer significant performance improvements, but substantial computational costs pose a challenge for practical application of such approaches. Here, we propose a new method for EEG source localization that combines: 1) covariance estimation for both source and measurement noises; 2) linear state-space dynamics; and 3) sparsity constraints, using 4) novel computationally efficient estimation algorithms. *Methods*: For source covariance estimation, we use a locally smooth basis alongside sparsity enforcing priors. For EEG measurement noise covariance estimation, we use an inverse Wishart prior density. We estimate these model parameters using an expectation–maximization algorithm that employs steady-state filtering and smoothing to expedite computations. *Results*: We characterized the performance of our method by analyzing simulated data and experimental recordings of eyes-closed alpha oscillations. Our sparsity enforcing priors significantly improved estimation of both the spatial distribution and time course of simulated data, while improving computational time by more than 12-fold over previous dynamic methods. *Conclusion*: We developed and demonstrated a novel method for improved EEG source localization employing spatial covariance estimation, dynamics, and sparsity. *Significance*: Our approach provides substantial performance improvements over existing methods using computationally efficient algorithms that will facilitate practical applications in both neuroscience and medicine.**

***Index Terms*—EEG, source localization problem, sparse prior models, observation noise.**

Manuscript received March 3, 2017; revised June 11, 2017 and August 4, 2017; accepted August 4, 2017. Date of publication September 14, 2017; date of current version May 18, 2018. This work was supported by the NIH Grants P41-EB015896 and 5R01-EB009048 to M. S. Hämäläinen and Grant DP2-OD006454 to P. L. Purdon. *(Elvira Pirondini and Behtash Babadi contributed equally to this work.) (Corresponding author: Patrick L. Purdon.)*

E. Pirondini is with the Institute of Bioengineering and the Center for Neuroprosthetics, Ecole Polytechnique Federale de Lausanne, and also with the Department of Radiology and Medical Informatics, University of Geneva.

B. Babadi is with the Department of Electrical and Computer Engineering, University of Maryland.

G. Obregon-Henao is with the Department of Anesthesia, Critical Care, and Pain Medicine, Massachusetts General Hospital, Harvard Medical School.

C. Lamus and W. Q. Malik are with the Department of Anesthesia, Critical Care, and Pain Medicine, Massachusetts General Hospital, Harvard Medical School, and also with the Department of Brain and Cognitive Sciences, Massachusetts Institute of Technology, Cambridge, MA.

M. S. Hämäläinen is with the Athinoula A. Martinos Center for Biomedical Imaging, Department of Radiology, Massachusetts General Hospital and Harvard Medical School.

P. L. Purdon is with the Department of Anesthesia, Critical Care, and Pain Medicine, Massachusetts General Hospital, and Harvard Medical School, Boston, MA (e-mail: patrickp@nmr.mgh.harvard.edu).

This paper has supplementary downloadable material available at http://ieeexplore.ieee.org.

Digital Object Identifier 10.1109/TBME.2017.2739824

## I. Introduction

Electroencephalography (EEG) and magnetoencephalography (MEG) record scalp electromagnetic fields that are generated by currents in the cerebral cortex. EEG and MEG make it possible to non-invasively record millisecond-level brain dynamics, and have been applied extensively in neuroscience to characterize sensory perception, cognition, language, and in clinical applications to characterize neurological disorders such as epilepsy. In these applications, it is crucial to determine, to the extent possible, where and when neurophysiological activity is occurring. Source localization methods seek to do just this, estimating both the spatial distribution and the time course of brain current sources from scalp EEG/MEG measurements. However, the source localization problem is ill-conditioned, meaning that the problem does not have a unique solution in the absence of additional constraints beyond the basic biophysics of EEG/MEG.

The earliest approaches to source localization used regularized least squares [1]–[5] under an assumption of temporal independence, to constrain solutions. More recently, Bayesian methods have been applied in a similar fashion to specify spatial constraints to solutions [6]–[10]. From a Bayesian perspective, many inverse algorithms can be viewed as a specific choice for the structure of the sources' prior probability density; in the Gaussian case this equates to specifying the prior source covariance [10]. From this collective work we learn that although regularizing constraints can produce unique solutions, the algorithms perform significantly better when the prior covariance structure can be refined and estimated from data [6], [10]–[12]. If the spatial covariance structure is important, so too is the temporal structure. As such, a number of methods have improved source estimates by modeling dynamics or temporal continuity in the underlying sources, using spatio-temporal priors [11], [13]–[20], linear state-space models [21]–[24], and neural mass models [25]. Most recently, there has been intense interest in developing sparse solutions to the EEG/MEG source localization problem [3], [26]–[31], justified in part by the concept that, in many cases, source generators for EEG/MEG are sparse compared to the large number of potential sources. In summary, three concepts–spatial source covariance estimation, dynamics, and sparsity–have emerged as key focus areas for developing improved EEG/MEG source localization algorithms.

New methods that combine these key ideas could offer significant performance improvements. However, practical application of these ideas and their combinations poses a number of challenges. Spatial source covariance estimation methods [6] and dynamic source localization algorithms [23] are computationally demanding, even more so when the spatial covariance is estimated within a dynamic model [12], [24]. Existing sparse algorithms are appropriate when the underlying neurophysiology supports highly focal sources [31]. However, sources can also be both sparse and spatially-distributed; methods to choose the spatial scale over which sparsity might apply remains an area of investigation [11], [32]–[35]. In EEG source localization, there is also the added complication that the covariance structure of the measurement noise must be specified. In MEG, the measurement noise covariance can be estimated from empty room recordings [36], but for EEG this is not possible since the measurement noise is observed primarily when subjects are being recorded. For evoked potential recordings, the measurement noise could be estimated from the pre-stimulus baseline signal [37], but this is not possible for spontaneous brain oscillations that do not have a well-defined baseline period.

In this paper, we describe a new method for EEG source localization that overcomes these issues, combining 1) covariance estimation for both source and measurement noise components, 2) linear state-space dynamics, and 3) sparsity constraints, using 4) novel estimation algorithms that are significantly faster than previous dynamic methods. A preliminary version of this work has been reported in [38]. For source covariance estimation, we use a locally-smooth basis representation similar to [11], but we identify the relevant covariance components using sparsity enforcing priors. We propose a novel method to estimate the EEG measurement noise covariance, using an inverse Wishart prior density [39] whose scale matrix is estimated using high-frequency components of the EEG signal that are typically dominated by noise. We estimate these model components using an expectation-maximization (EM) algorithm that employs steady-state filtering and smoothing for the E-step, which reduces computational time by an order of magnitude over previous similar algorithms. We evaluate the performance of our method using simulated data and experimental recordings of resting state alpha oscillations. We show that our dynamic state-space model with spatial sparse priors performs better, in terms of source estimation and computational efficiency, compared to previous dynamic methods.

## II. Materials and Methods

### A. State Space Model

We describe the state space model for EEG signals; the same model applies to MEG and combined EEG/MEG recordings. We denote the electric potentials recorded by the EEG sensor $i$ at time $t$ by $y_{i,t}$ for all $i = 1, 2, \ldots, N_y$ and $t = 1, 2, \ldots, T$. Let $y_t := [y_{1,t}, y_{2,t}, \ldots, y_{N_y,t}]'$ be the $N_y \times 1$ vector of observations at time instant $t$, where $N_y$ denotes the number of EEG sensors. Let $x_{i,t}$ denote the source amplitude of the current dipole $i$ at time $t$, and let $x_t := [x_{1,t}, x_{2,t}, \ldots, x_{N_x,t}]'$ be the $N_x \times 1$ vector of dipole sources distributed on the cortex, representing cortical currents at time $t$. $N_x$ denotes the number of dipole sources. We assume that the current dipoles are oriented normal to the cortical surface [37]. A typical value of $N_y$ is in the range of 32–256, whereas $N_x$ can vary from hundreds to thousands depending on how the source space is configured.

The EEG observation model can be expressed as:

$$y_t = G x_t + v_t, \tag{1}$$

where $G$ is the $N_y \times N_x$ lead field gain matrix, denoting the linear mapping between the cortical dipole activity and the sensor measurements. The gain matrix $G$ can be estimated using a quasi-static approximate solution to the Maxwell's equations [36]. All components of uncertainty independent of $x_t$, such as the instrument noise at the sensors or environmental disturbances, are captured by the $N_y \times 1$ vector $v_t$ at time $t$. The observation noise $v_t := [v_{1,t}, v_{2,t}, \ldots, v_{N_y,t}]'$ vector can be modeled as a Gaussian random vector with mean zero and covariance matrix $C$ that is independent and identically distributed across time.

In a static model, the sources can be assumed to be generated by a Gaussian process with covariance matrix $Q$. In a dynamic (state-space) model, the spatiotemporal connections between sources can be represented by a first order autoregressive model with nearest-neighbor interactions [12]. The choice of a first order autoregressive model is justified by evidence from previous neurophysiology, neuroanatomy, and neuroimaging studies that suggest that the cortical activation is a distributed spatiotemporal dynamic process within small local neighborhood [12]. In this model, the source amplitude of dipole $i$ at time $t$ is a linear combination of its activity at time $t-1$ as well as those of its nearest neighbors, perturbed by a state noise variable $w_{i,t}$ that accounts for components of uncertainty affecting the temporal evolution of cortical currents:

$$x_{i,t} = \lambda[a_i x_{i,t-1} + (1 - a_i) \sum_{j \in N_1(i)} d_{i,j} x_{j,t-1}] + w_{i,t}, \tag{2}$$

where $N_1(i)$ is the set of nearest neighbors of dipole $i$, and $d_{i,j}$ denotes the normalized inverse distance between dipoles $i$ and $j$. The scalar parameter $a_i \in [0, 1]$ is a weighting factor, and $\lambda$ is a positive scalar sufficiently close to 1, ensuring the stability

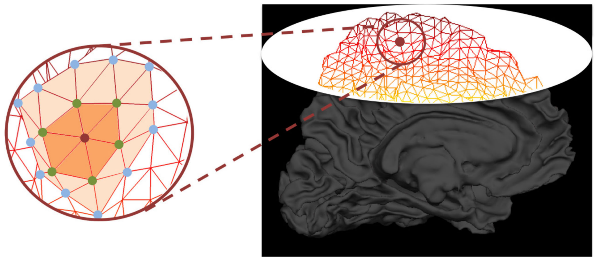

Fig. 1. Cortical surface reconstructed from MRI using Freesurfer [40], where the upper portion is represented by its triangulated mesh of dipoles. A zoomed-in segment of the triangulation is shown on the left and it highlights the local topology of the source space. The brown vertex is the central dipole, and the first and second neighbors are represented by green and blue vertices, respectively. The local topology of the source space is employed in the construction of matrices $F$ and $B$ (see (2)–(4)).

of the autoregressive model. We will explain our choices of $\lambda$ and $a_i$ in Section II-G.

Equation (2) can be expressed in the following compact form,

$$x_t = Fx_{t-1} + w_t, \tag{3}$$

where the $N_x \times N_x$ matrix $F$, referred to as the transition matrix, captures the spatial interactions in the autoregressive model (See Fig. 1), and the state noise $w_t := [w_{1,t}, w_{2,t}, \ldots, w_{N_x,t}]'$ represents inputs that drive the cortical currents. We model the state noise vector $w_t$ as a Gaussian process with covariance matrix $Q$, independent and identically distributed across time, and independent of the measurement noise $v_t$. The initial state vector $x_0$ is assumed to be a Gaussian random vector with mean zero and covariance $Q_0$. Note that the static model can be regarded as a special case of the dynamic model where $F$ is set to zero.

In previous works, the source covariance $Q$ has been modeled with a diagonal structure [1], [6], [12]. However, this diagonal structure treats the sources as independent across the cortex, and fails to account for the spatial dependencies between the sources and in the underlying state noise. We generalize the structure of $Q$ by specifying off-diagonal elements that can capture spatial dependencies between the sources and in the state noise process. To do this, we construct a basis for representing $Q$ that is informed by the local topology of the source space [11].

Let $B$ be a $N_x \times N_x$ matrix with elements:

$$(B)_{i,j} = \begin{cases} 1 & \text{if} \quad i = j \\ \delta_1 d_{i,j} & \text{if } j \in N_1(i) \\ \delta_2 d_{i,j} & \text{if } j \in N_2(i) \\ 0 & \text{otherwise} \end{cases}, \tag{4}$$

where $N_1(i)$ and $N_2(i)$ denote the set of first and second nearest neighbors of the dipole $i$, respectively, and $\delta_1$ and $\delta_2$ are two positive scaling constants (See Fig. 1). Let $\{q_1, q_2, \ldots, q_{N_x}\}$ be the a set of orthonormal basis vectors spanning the range of $B$. We restrict the structure of $Q$ to the set of symmetric matrices of the following form:

$$Q(\theta) = \sum_{i=1}^{N_x} \theta_i q_i q_i'. \tag{5}$$

where $\theta_i$ are the expansion coefficients, and $\theta := [\theta_1, \theta_2, \ldots, \theta_{N_x}]'$.

### B. Priors on the State-Space Parameters

In theory all the parameters in our model have uncertainties. However, some of them can be fixed a priori based on knowledge of the system under investigation. For instance, the transition matrix $F$ is constructed as described above (see Section II-A) and the lead field matrix $G$ is computed using a boundary-element model based on magnetic resonance images (MRI) (see Section II-I).

The covariance matrices $\{Q, Q_0, C\}$, on the other hand, have to be estimated from the data. As discussed in the introduction, EEG/MEG source activity can be viewed as sparse compared to the large number of potential sources, and this sparsity can be represented in terms of a sparse prior source covariance. To estimate a sparse covariance, we use sparsity-enforcing priors on the coefficients $\theta_i$ that parameterize $\{Q\}$ in (5). The sparse priors can be formulated in a number of ways. We describe here three forms of sparse priors on $\theta_i$, namely, the Laplace prior,

$$p(\theta) = \gamma^{N_x} \prod_{i=1}^{N_x} \exp(-\gamma\theta_i), \tag{6}$$

the Jeffreys prior [41],

$$p(\theta) = \prod_{i=1}^{N_x} \frac{1}{|\theta_i|}, \tag{7}$$

and log-sum approximation to the zero-norm log-prior [42],

$$p(\theta) = \prod_{i=1}^{N_x} \frac{c_0}{(1+\gamma|\theta_i|)^2}. \tag{8}$$

The parameter $\gamma$ in (6) and (8) can be tuned in order to maintain the appropriate scaling of the expansion coefficients with the observation data (see Section II-G for details). The normalization constant $c_0$ in (8) does not need to be explicitly computed, since it does not couple with the parameters $\theta_i$ in the log-likelihood form. For brevity, we denote the prior given in (8) by the name log-sum prior. In Section II-E will derive expressions for estimating $\theta_i$ under each of these priors, and will compare source localization performance using each prior (see Table I and Results).

As discussed in the Introduction, the characterization of the observation noise is a crucial requirement for source localization, and is particularly challenging in EEG recordings of spontaneous brain oscillations, because the observation noise cannot be temporally separated from the overlying neurophysiological signal. Therefore, in our approach we consider the observation noise covariance as an unknown parameter. We use the inverse Wishart distribution [39] as a prior density for the observation noise covariance $C$:

$$p(C) = \frac{|\Psi|^{\frac{\nu}{2}}}{2^{\frac{\nu N_y}{2}} \Gamma_{N_y}\left(\frac{\nu}{2}\right)} |C|^{-\frac{\nu+N_y+1}{2}} \exp\left(-\frac{1}{2}\text{tr}(\Psi C^{-1})\right), \tag{9}$$

TABLE I
ABBREVIATIONS FOR THE DIFFERENT SOURCE LOCALIZATION ALGORITHMS EVALUATED IN THE RESULTS SECTION

| Model \ Prior | Inverse Gamma [12] | Laplace Eqs.(6) and (17) | Jeffreys Eqs.(7) and (18) | log-sum Eqs.(8) and (19) |
|---|---|---|---|---|
| Static | sMAP–EM | sLAP | sJEFF | sLOG |
| Dynamic | dMAP–EM | dLAP | dJEFF | dLOG |

where $\Psi$ is a $N_y \times N_y$ positive definite matrix, and $\nu$ is an order parameter. The inverse Wishart prior is commonly employed to regularize covariance estimates in order to achieve robustness [39]. We set the scale matrix $\Psi$ and degrees of freedom $\nu$ based on the observed data as described in Section II-G.

### C. Parameter Estimation Using a Maximum a Posteriori Expectation–Maximization Algorithm

Given the state space model as defined above, we can obtain a solution to the source localization problem by estimating 1) the source covariance matrix $Q$ parameterized by the expansion coefficients $\theta_i$, 2) the observation noise matrix $C$, and 3) the sequence of source amplitudes $\{x_t\}_{t=1}^T := [x_1, x_2, \ldots, x_{N_T}]$.

For the parameters $\theta_i$ and $C$ we use a Maximum *a Posteriori* (MAP) approach:

$$\left\{\widehat{\theta}, \widehat{C}\right\}_{\text{MAP}} := \underset{\theta, C}{\text{argmax}} \quad p\left(\theta, C | \{y_t\}_{t=1}^T\right) \tag{10}$$

where $p\left(\theta, C | \{y_t\}_{t=1}^T\right)$ is the posterior density of the parameters $\left\{\theta, C\right\}$ conditioned on the set of measurements $\{y_t\}_{t=1}^T$.

For the source amplitudes, the conditional mean of the state vector at time $t$ given the full set of measurements $\{y_t\}_{t=1}^T$ and the MAP estimate $\left\{\widehat{\theta}, \widehat{C}\right\}_{\text{MAP}}$, i.e., the empirical Bayes estimate, is denoted by:

$$x_{t|T} := \mathbb{E}\left\{x_t \middle| \{y_t\}_{t=1}^T, \left\{\widehat{\theta}, \widehat{C}\right\}_{\text{MAP}}\right\}, \tag{11}$$

where the subscript notation $x_{t|T}$ denotes that the conditioning at time $t$ is over the full set of measurements from time 1 to $T$.

Once we obtain the MAP estimate of the parameters $\left\{\widehat{\theta}, \widehat{C}\right\}_{\text{MAP}}$, the empirical Bayes estimate of the source amplitudes (11) can be readily obtained using the well-known Kalman Filter (KF) [43] and Fixed Interval Smoother (FIS) algorithms [44].

To obtain the MAP estimate of the parameters $\{\theta, C\}$, we derive an Expectation-Maximization (EM) algorithm, treating the sequence of measurement $\{y_t\}_{t=1}^T$ and the state vector $\{x_t\}_{t=0}^T$ as the *complete data* and iterating the E-step followed by an M-step until convergence is achieved [12].

In the *r*th iteration of the E-step, we compute the conditional expectation of the complete data log-posterior, given the observed data $\{y_t\}_{t=1}^T$, the previous estimates of the parameters $\{\theta, C\}^{(r-1)}$, and with an added term for the log-prior density:

$$\begin{aligned}
&U(\{\theta, C\} \,|\, \{\theta, C\}^{(r-1)}) = \\
&-\frac{1}{2}\left\{c_1 + \log|Q_0^{(r-1)}| + \text{tr}\left[Q_0^{-1(r-1)}(P_{0|T}^{(r)} + x_{0|T}^{(r)} x_{0|T}^{(r)\prime})\right]\right\} \\
&-\frac{1}{2}\left\{c_1 T + T\log|Q| + \text{tr}\left[Q^{-1}\Omega^{(r)}\right]\right\} \\
&-\frac{1}{2}\left\{c_2 T + T\log|C| + \text{tr}\left[C^{-1}\Sigma^{(r)}\right]\right\} \\
&+\log p(\theta) + \log p(C),
\end{aligned} \tag{12}$$

where $c_1$ and $c_2$ are constants not depending on $\{\theta, C\}$, $P_{t|T}^{(r)} = \text{Cov}(x_t | y_{k}{}_{k=1}^T, \theta, C^r)$ is the conditional covariance, and $\Omega^{(r)}$ and $\Sigma^{(r)}$ are given by [12]:

$$\begin{aligned}
\Omega^{(r)} := \sum_{t=1}^{T} \Bigg\{ &\left(P_{t|T}^{(r)} + x_{t|T}^{(r)} x_{t|T}^{(r)\prime}\right) \\
&- \left(P_{t|T}^{(r)} (P^{-1}{}_{t|t-1}^{(r)})' F (P_{t-1|t-1}^{(r)})' + x_{t|T}^{(r)} x_{t-1|T}^{(r)\prime}\right) F' \\
&- F\left(P_{t-1|t-1}^{(r)} F' P^{-1}{}_{t|t-1}^{(r)} P_{t|T}^{\prime(r)} + x_{t-1|T}^{(r)} x_{t|T}^{(r)\prime}\right) \\
&+ F\left(P_{t-1|T}^{(r)} + x_{t-1|T}^{(r)} x_{t-1|T}^{(r)\prime}\right) F' \Bigg\},
\end{aligned}$$

and

$$\Sigma^{(r)} := \sum_{t=1}^{T} \left\{ \left(y_t - G x_{t|T}^{(r)}\right)\left(y_t - G x_{t|T}^{(r)}\right)' + G P_{t|T}^{(r)} G' \right\}. \tag{13}$$

We use the Kalman Filter (KF) [43] to calculate the predicted $\left(P_{t|t-1}^{(r)}\right)$ and filtered $\left(P_{t|t}^{(r)}\right)$ covariance matrices, and use the Fixed Interval Smoother (FIS) [44] to calculate the smoothed state estimates $\left(x_{t|T}^{(r)}\right)$ and smoothed covariance matrix $\left(P_{t|T}^{(r)}\right)$ (See the appendix and [12] for details). The estimated sequence of source amplitudes $\{\hat{x}_t\}_{t=1}^T$ correspond to the smoothed state estimates.

### D. Steady-State Versions of the Kalman Filter and Fixed-Interval Smoother

The EM algorithm described above has a high computational cost because each E-step requires estimation of filtered and smoothed covariance matrices, as well as smoothed state estimates. The covariance matrices are particularly costly to handle, because at each time step, $N_x \times N_x$ matrices must be multiplied and inverted, and then must be stored for use in the FIS. In order to reduce the computational and storage costs of this algorithm, we introduce steady-state versions of the Kalman Filter (SS-KF) and Fixed Interval Smoother (SS-FIS) [45], [46]. We use the SS-KF and SS-FIS to replace the predicted, filtered, and smoothed covariance matrices at each time point with steady-state versions that are computed and stored only once per EM iteration.

We denote the steady-state predicted state covariance, filtered state covariance, and Kalman gain, respectively, as:

$$\begin{aligned} P^{-(r)} &:= \lim_{t\to\infty} P^{(r)}_{t|t-1}, \\ P^{(r)} &:= \lim_{t\to\infty} P^{(r)}_{t|t}, \\ K^{(r)} &:= \lim_{t\to\infty} K^{(r)}_{t}. \end{aligned} \tag{20}$$

The steady state values $P^{-(r)}$, $P^{(r)}$, and $K^{(r)}$ can be computed using an efficient nonrecursive procedure based on the solution of the discrete algebraic Riccati equation (DARE) using the MacFarlane-Potter-Fath eigenstructure method (See [45] and [46] for details). By finding the solution to the Riccati equation, we can compute the Kalman gain and the predicted covariance as:

$$\begin{aligned} K^{(r)} &= P^{(r)}G'(GP^{(r)}G' + C^{(r)})^{-1}, \\ P^{-(r)} &= (I - K^{(r)}G)P^{(r)}. \end{aligned} \tag{15}$$

The FIS gain given by $J^{(r)}_t = P^{(r)}_{t|t}F'P^{(r)-1}_{t+1|t}$ and the smoothed covariance given by $P_{t|T} = P^{(r)}_{t|t} + J^{(r)}_t(P^{(r)}_{t+1|T} - P^{(r)}_{t+1|t})J'^{(r)}_t$ are continuous functions of the predicted and filtered state covariance matrices from the KF. Consequently, steady-state values for these quantities can also be defined:

$$\begin{aligned} J^{(r)} &:= \lim_{t\to\infty} J^{(r)}_t = P^{(r)}F'P^{-(r)} \\ P^{+(r)} &:= \lim_{t\to\infty} P^{(r)}_{t|T} = P^{(r)} + J^{(r)}(P^{(r)} - P^{-(r)})J'^{(r)}. \end{aligned} \tag{16}$$

Since the smoothed state estimates $x^{(r)}_{t|T}$ only depend on the smoother gain (See the appendix), we can calculate approximate values denoted by $\tilde{x}^{(r)}_{t|T}$ using the SS-FIS.

### *E. M-step*

After each E-step, we update the unknown model parameters in the subsequent M-step, which is achieved by maximizing the function $U(\{\theta, C\} \,|\, \{\theta, C\}^{(r-1)})$ (12) with respect to the parameters $\{\theta, C\}$.

For each of the prior densities for the state covariance parameters (6)–(8), the maxima are achieved at:

$$\theta^{(r)}_n = \frac{\sqrt{T^2 + 8q'_n\Omega^{(r)}q_n\gamma} - T}{4\gamma}, \text{ for the Laplace prior,} \tag{17}$$

$$\theta^{(r)}_n = \frac{q'_n\Omega^{(r)}q_n}{T+2}, \text{ for the Jeffreys prior,} \tag{18}$$

and in the expression in equation (19) at the bottom of the page, for the log-sum prior for $n = 1, 2, \ldots, N_x$. Similarly, the observation noise covariance can be updated in the M-step using the following expression:

$$C^{(r)} = \frac{\Sigma^{(r)} + \nu\Psi}{T + \nu + N_y + 1}. \tag{20}$$

Equations (17)–(20) reveal the trade-offs between the empirical estimates (i.e., $\Omega^{(r)}$ and $\Sigma^{(r)}$) and priors (i.e., $\gamma$, $\nu$, and $\Psi$) on the parameters: if the empirical estimates are reliable (i.e., high SNR and no model mismatch) the contribution of the prior is suppressed, whereas when the empirical estimates of $Q$ and $C$ are ill-conditioned, the prior values dominate the estimates and thereby result in estimation stability.

The EM algorithm iterates between the E-steps and M-steps until the log posterior density of the parameters evaluated at $\left\{\theta^{(r)}, C^{(r)}\right\}$ given by:

$$\begin{aligned} &\log p(\theta^{(r)}, C^{(r)} | \{y_t\}^T_{t=1}) = \log p\big(\{y_t\}^T_{t=1} | \left\{\theta^{(r)}, C^{(r)}\right\}\big) \\ &+ \log p(\theta^{(r)}) + \log p(C^{(r)}) - \log p(\{y_t\}^T_{t=1}) \end{aligned} \tag{21}$$

reaches an asymptote at some iteration $r$ [12].

### *F. Source Space*

Under a distributed source model, cortical currents can be represented using a dense sampling of current dipoles, with as many as 10,000 or more dipoles covering each cortical hemisphere. However, the number of independent sources that can be localized is in principle limited by the number of EEG sensors. Moreover, the spatial resolution of EEG is limited by factors such as the low conductivity of the skull and the distance of the sources from the sensors [37]. If the source space is large, source estimation, particularly using a dynamic model, can be computationally burdensome or infeasible. On the other hand, if the number of dipoles in the source model is reduced significantly, the resulting coarse spatial sampling may not appropriately capture the geometry of the gyri and sulci [47].

To achieve a balance between an accurate representation of source geometry and manageable computational complexity, we employed a reduced-dimension source space consisting of densely-sampled homogeneous cortical patches [47]. We con-

$$\theta^{(r)}_n = \frac{(q'_n\Omega^{(r)}q_n\gamma - T)/2 + \sqrt{\left(q'_n\Omega^{(r)}q_n\gamma - T\right)^2/4 + 2\gamma\left(2 + \frac{T}{2}\right)q'_n\Omega^{(r)}q_n}}{\gamma(4+T)}, \tag{19}$$

structed the source space using cortical patches of average diameter 1.25 cm $+/-$ 0.18 $\mathrm{cm}$ tiling the entire cortical mantle, consistent with the presumed centimeter-level spatial resolution of EEG [37]. The resulting source space had 1284 cortical patches. Each patch was composed of many densely sampled dipoles, with a total of $\sim 300,000$ dipoles across all cortical patches [31]. We treated the cortical currents within each patch as having a constant value (i.e., single dipole), summing the contributions across the densely sampled dipoles. Since the orientation of the current generators of the electromagnetic field, i.e., the apical dendrites of pyramidal cells, is perpendicular to the cortical surface [37], we constrained the dipoles within each patch to be oriented normal to the cortical surface. This allowed us to represent the current in each patch using a single state parameter.

## G. Parameter Settings and Algorithm Initialization

We constructed the matrix $B$ given in (4) using $\delta_1 = 0.5$ and $\delta_2 = 0.25$, and the transition matrix $F$ to incorporate nearest-neighbor interaction between source patches. In both cases, the distances between the centroids of patches were calculated using the triangular tessellation of the cortical surface. We set the value of $a_i$ to 0.5 to account for the balance between the past activation in the central dipole and its neighbors, and λ to 0.95. For these parameter choices, the modulus of the largest eigenvalue of $F$ is strictly less than 1, ensuring that the source model dynamics are stable.

We based our estimate of the initial observation noise covariance on the sample covariance of the EEG data after high-pass filtering above 50 Hz, since in our experience, noise sources tend to predominate at frequencies >50 Hz. The initial observation noise covariance was therefore set to $C_0 = 2 * COV(\hat{y}_i, \hat{y}_j)$, where $\hat{y}_i$ and $\hat{y}_j$ represent the EEG data high-pass filtered above 50 Hz, and where the factor of 2 accounts for noise occupying frequencies <50 Hz. We set the parameters of the inverse Wishart distribution, $\Psi$ and $\nu$, to match the estimate of the initial observation noise covariance –i.e., $\Psi$ was set equal to $C_0$ and $\nu$ was set to the length of the signal. We chose the initial state noise covariance $Q(\theta^{(0)})$ to be $Q(\theta^{(0)}) = 0.1 Q_0$, with $Q_0 = \sigma_x^2 I$, where

$$\sigma_x^2 := \mathrm{SNR}\frac{\mathrm{tr}(C_0)}{\mathrm{tr}(GG')}, \tag{22}$$

to approximate the power signal-to-noise ratio (SNR) of the measurements.

Finally, we chose the parameter $\gamma$ for the Laplace prior to be the average of the $N_x$ quantile estimates, given by:

$$\gamma = \frac{-\sum_{i=1}^{N_x} \log(1-(i-1/2)/N_x)}{\mathrm{tr}(Q_0)}. \tag{23}$$

Note that for large values of $N_x$, $\gamma \approx \frac{1}{\sigma_x^2}$. Similarly, for the log-sum prior (with undefined mean), we choose $\gamma$ to be inversely proportional to the initial state variances:

$$\gamma = \frac{N_x}{\mathrm{tr}(Q_0)}. \tag{24}$$

## H. Summary of the Algorithms

Table I shows a summary of the key features of the algorithms described here and in previous work, and provides nomenclature that will be used in the remainder of the text.

For brevity, in the next sections, we refer to sMAP–EM and dMAP–EM as sMAP and dMAP, respectively. All the algorithms were implemented in Matlab (The MathWorks, Natick, MA) running on a dual 6-core Linux workstation at 2.67 GHz with 24 GB RAM.

## I. Experimental Recordings

Following approval from the Massachusetts General Hospital Human Research Committee, the EEG data were recorded using a 64-channel EEG cap (BrainAmp MRPlus, BrainProducts, GMBH) from three human subjects. The recordings were acquired at a sampling frequency of 5 kHz. The data were re-referenced to a common average reference, down-sampled to 200 Hz, and filtered above of 0.1 Hz off-line. The positions of the EEG electrodes and fiduciary points (nasion and periauricular points) were digitized using the 3Space Isotrak II System, and aligned to each subject's structural MRI prior to forward model construction. We computed the forward model gain matrices $G$ for each subject using the MNE software (http://martinos.org/mne/), using a realistic 3-layer boundary element method (BEM) model based on high-resolution structural MRI obtained for each subject (T1 mprage, 1.3 mm slice thickness, $1.3 \times 1$-mm in-plane resolution, TR/TE = 2530/3.3 ms, 7° flip angle, Siemens Trio 3 Tesla MR scanner). The three layers modeled were scalp, brain, and skull with conductivity values of 0.3 S/m for scalp and brain, and 0.006 S/m for the skull (i.e., default values proposed by MNE). Dipoles within 5 mm of the inner-skull bounding surface were discarded from the computation of the gain matrix $G$ to avoid numerical inaccuracies that could potentially affect the source activity estimates [31].

## J. Design of Simulation Studies

We simulated 10 Hz sinusoidal oscillations, $1s$ in duration, with a sampling frequency of 200 Hz, over a patch of cortical activity located in the pre-frontal cortex of the left hemisphere, using a density sampled cortical source space of $\sim 300,000$ dipoles. The patch of activity was composed of $\sim$3000 dipoles (i.e., 12 cortical patches, see Section II-F) with spatially uniform amplitudes (Fig. 4). To generate the simulated 64-channel EEG recordings, we used the observation model given by (1) with the measurement noise covariance estimated using the MNE software from experimental EEG data and the gain matrix $G$ from one of the three subjects included in the study (see Section II-I). In order to avoid the so-called "inverse-crime", we used a different gain matrix for source localization than the one used to generate the simulated data. Specifically, for the simulation, we used a lead field matrix computed over a density sampled cortical source space of $\sim 300,000$ dipoles. For source localization, we used a gain matrix computed over a reduced-dimension source space consisting of densely-sampled homogeneous cortical patches (see Section II-F). Finally, we scaled the dipole

TABLE II
COMPARISON OF KF AND FIS TO SS-KF AND SS-FIS, RESPECTIVELY (MEAN +/- STD. DEV. OVER 25 REALIZATIONS)

| Kalman \ Performances | AUC | RMSE inside | RMSE outside | Energy | Time (min) |
|---|---|---|---|---|---|
| KF and FIS | 0.9809 ± 0.0018 | 0.643 ± 0.0006 | 0.020 ± 0.0006 | 0.84 ± 0.01 | 125.10 ± 2.70 |
| SS-KF and SS-FIS | 0.9805 ± 0.0016 | 0.637 ± 0.0004 | 0.022 ± 0.0008 | 0.82 ± 0.01 | 10.50 ± 0.02 |

The standard and steady-state versions of these algorithms have very similar AUC, normalized RMSE inside and outside the active region, and localized energy ratio values. However, the computation time for the steady-state algorithms is significantly lower.

amplitudes to achieve an SNR of 3 (typical for EEG recordings) [36]. We also performed a number of additional simulations, reported in the Supplementary Material Sections I–III, featuring activity in different cortical areas, with multiple distant yet spatially-correlated sources, and with lower SNR values, to assess the robustness of our method.

### K. Performance Measures

In previous studies, we found that sMAP and dMAP improved source localization performance compared to the $L_2$ Minimum Norm Estimate [1] and the Fixed Interval Smoother (FIS), in terms of spatial localization accuracy, temporal tracking, posterior error covariance, and RMSE and ROC measures [12]. We therefore focus our performance analyses on comparisons of our new sparse methods under static (sLAP, sJEFF, sLOG) and dynamic models (dLAP, dJEFF, dLOG) with the previously established sMAP and dMAP models.

In order to evaluate the performance of our proposed source localization algorithms on the simulated data, we used three performance measures: 1) the root mean square error (RMSE), both inside and outside the active region, normalized by the root mean square (RMS) of the entire simulated patch activity; 2) the localized energy ratio; and; 3) the receiver operating characteristic (ROC) curve. We describe these performance measures in detail below.

The expression for the normalized RMSE is given by:

$$\mathrm{RMSE}_i := \frac{\sqrt{\frac{\sum_{t=1}^{T}\left(\hat{x}_{i,t}-x_{i,t}^{(\mathrm{SIM})}\right)^2}{T}}}{\sqrt{\frac{\sum_{i\in\mathcal{I}}\sum_{t=1}^{T}\left(x_{i,t}^{(\mathrm{SIM})}\right)^2}{\mathcal{I}T}}} \tag{25}$$

where $\hat{x}_{i,t}$ and $x_{i,t}^{(\mathrm{SIM})}$ denote the estimated (i.e., the smoothed state estimates) and the simulated values of the $i$th patch at time $t$, and $\mathcal{I}$ denotes the set of indices corresponding to the patches in the active region.

We define the localized energy ratio as the ratio of the energy of the estimates in the actual active patches to that of the entire source space [31]:

$$E = \frac{\sum_{i\in\mathcal{I}}\sum_{t=1}^{T}|\hat{x}_{i,t}|^2}{\sum_{i=1}^{N_x}\sum_{t=1}^{T}|\hat{x}_{i,t}|^2}. \tag{26}$$

Finally, we compute the ROC curve, representing the sensitivity/specificity trade-off, by evaluating the detection probability and the false alarm probability given a threshold, $c$, on the amplitude of the estimates, accounting for the null hypothesis. The null hypothesis ($H_0$) is true when the $i$th dipole source at time $t$ equals zero ($x_{i,t}^{(SIM)} = 0$) [12]. We estimate the detection probability as the fraction of events where an active source was correctly detected, i.e, when the dipole source estimate was considered active ($|\hat{x}_{i,t}| > c$), given the presence of an active source ($x_{i,t}^{(SIM)} \neq 0$), with respect to the total duration of $T$ and all sources $N_x$. Similarly, we estimate the false alarm probability as the proportion of events where the source estimate was deemed to be active but the underlying true source was inactive ($x_{i,t}^{(SIM)} = 0$), with respect to the total duration of $T$ and all sources $N_x$.

## III. RESULTS

### A. Characterization of Steady State Algorithms

To evaluate our proposed steady-state algorithms, we compared the performance of the KF and FIS to their steady-state counterparts, the SS-KF and SS-FIS (Table II). For brevity, we present only the performance comparison for the dLAP algorithm; the Jeffreys and log-sum algorithms showed very similar performance. The simulation and estimation were repeated 25 times with different realizations of the observation noise. The computation time was estimated as the average over all 25 realizations.

The performance differences between the KF/FIS and their steady-state versions were small. The KF and FIS had a slightly better RMSE outside the active region compared to the SS-KF and SS-FIS. However, the SS-KF and SS-FIS reduced the computational time by 12-fold compared to the standard versions of the algorithm.

Fig. 2(a) shows the smoothed state estimates $\hat{x}_{t|T}$ and $\tilde{x}_{t|T}$ for KF and FIS and for SS-KF and SS-FIS, respectively, for two exemplary patches inside and outside the active region following the convergence of the EM algorithm. The two estimates only deviate for the first approximately 10 ms, and are virtually identical thereafter. To quantify the temporal performance in greater detail, we computed the histogram of the time it takes to have a normalized deviation of less than 5% between the KF and FIS, and SS-KF and SS-FIS, over the entire source space for one realization of the simulation (Fig. 2(b)):

$$\frac{(\tilde{x}_{i,t} - \hat{x}_{i,t})^2}{\frac{1}{T}\sum_{t=1}^{T}\tilde{x}_{i,t}^2}. \tag{27}$$

For more than half of the patches, the required time for the SS-KF and SS-FIS to achieve a normalized deviation of at most 5% compared to KF and FIS was less than 10 ms. This level of performance is similar to other recent applications of steady-state Kalman filters [45].

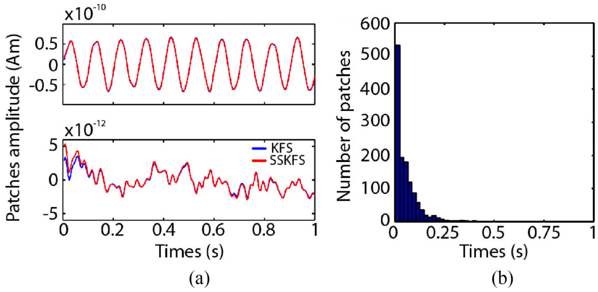


Fig. 2. Comparison between KF and FIS, and SS-KF and SS-FIS. (a) The estimated activity from two patches, one inside (top panel) and one outside (bottom panel) the active region, obtained using KF and FIS (blue lines) and SS-KF and SS-FIS (red lines). The estimates of KF/FIS and of their steady-state versions are nearly identical for the patch inside the active region. For the patch outside the active region, the SS-KF and SS-FIS estimate has a normalized deviation of more than 5% from the KF/FIS estimate for only the first 10 ms of the data, and closely follows the KF/FIS estimate afterwards. (b) Histogram of the time required for the SS-KF and SS-FIS estimate to achieve a normalized deviation of less than 5% from the KF/FIS estimate for all the patches in the source space. For more than 50% of the patches, the deviation time is less than 10 ms.

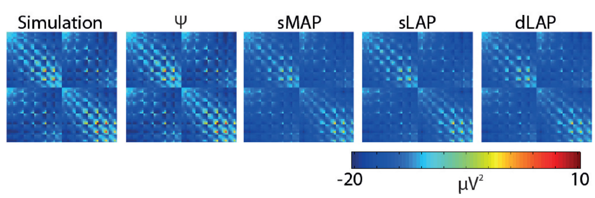


Fig. 3. Estimated observation noise covariance matrices. The first panel shows the observation noise covariance matrix used to generate the simulated data. The units of the color bar are $\mu V^2$. The second panel shows the $\Psi$ matrix. The third through fifth columns show the estimated observation noise covariance matrices for the sMAP, sLAP, and dLAP algorithms, respectively. The estimated covariance matrices under all three methods are consistent with the covariance of the data generating process. Note that due to regularization, a combination of the initial estimate $\Psi$ and the empirical estimate from the EM algorithm shapes the structure of the final estimate of $C$, in both the simulated and experimental data analysis results. We report here the estimates from three methods for brevity. However, all the methods showed a similar ability to recover the main structure of the original observation noise covariance.

For the remainder of the simulation studies, as well as the analysis of experimental data, we used the SS-KF and SS-FIS for all the dynamic methods.

### B. Estimation of the Observation Noise

We next evaluated our algorithm for estimating both the scale and the structure of the observation noise covariance. As illustrated in Fig. 3, we were able to appropriately capture the structure of the noise covariance using the inverse Wishart prior. Both the static and dynamic models underestimated the total variance in the observation noise matrix by about ~36%. However, as the following results reveal, the loss in the total variance of the estimated observation noise covariance had a negligible effect on the source localization performance.

### C. Results: Simulation Studies

First, we characterized the performance of our method by analyzing simulated data. The static models, particularly sMAP, produced estimates that appeared to be more focal than the true active region (Fig. 4), with amplitudes dramatically lower than the actual simulated signals (Fig. 5). Moreover, these models could produce strong activity outside the actual active region. The dynamic models, on the other hand, produced estimates with a spatial spread comparable to the actual activity, with estimated time courses that more closely matched the simulated signals, notably in the amplitude of the signal. In both static and dynamic models, the use of a sparse empirically-tailored basis led to improvements over the sMAP and the dMAP, respectively, in terms of both the spatial spread and the estimation of the amplitude.

Normalized RMSE and localized energy ratio values were consistent with these observations (Fig. 6). Among the static models, the sLAP was the one that provided the lowest RMSE inside the simulated active region, with a value of 0.84, which translates into an improvement of ~9% compared to the sMAP algorithm (Fig. 6(a)). The sMAP algorithm exhibited a better RMSE performance outside the active region, with an improvement of ~16% over sLAP and sLOG, and ~13% over sJEFF (Fig. 6(b)). However, sMAP achieved the lowest value of localized energy ratio among the different algorithms (~3 times smaller than those of the sparse static models and ~10 times smaller than those of the dynamic models, Fig. 6(c)). In other words, the sMAP algorithm tended to spread the source energy over the entire cortical space, instead of localizing it over the actual region of activity.

Dynamic models were significantly better at capturing the activity inside the true area of activation compared to static models. They achieved a localized energy ratio about ~4 times higher than those of their static counterparts (Fig. 6(c)). The dLAP model showed the lowest RMSE inside the active region with a value of 0.64, which represents an improvement of ~11% compared to dMAP (Fig. 6(a)).

ROC measures showed similar performance trends (Fig. 7). The static models exhibited the lowest initial slope as well as AUC. In particular sMAP (magenta trace, top panel) had the lowest detection rate as a function of false alarm probability compared to all other methods. The use of an empirically-tailored basis and sparse priors in static models made it possible to achieve ROC performance similar to those of the dynamic models (about 0.94). The highest value of AUC was achieved using the sJEFF (about 0.95). The ROC curves show that the dynamic models outperformed their static counterparts. Among them, the dLAP (red line), dJEFF (dark green line), and dLOG (blue line) achieved the highest AUC (about 0.98) as well as the highest initial slope. The dynamic models with sparse priors and an empirically-tailored basis (dLAP, dJEFF, and dLOG) were similar in their localization accuracy and computational time (see Table III).

In order to further evaluate the performance of our proposed algorithms, we performed additional simulation studies: (1) a patch of activity simulated over the somatosensory cortex; (2) performance against varying SNR levels; and (3) performance under the presence of a non-local second source whose activity is related to the original source in a cross-regressive fashion. We obtained results consistent with our simulation of the pre-frontal activity (see Supplementary Material Section I– III).

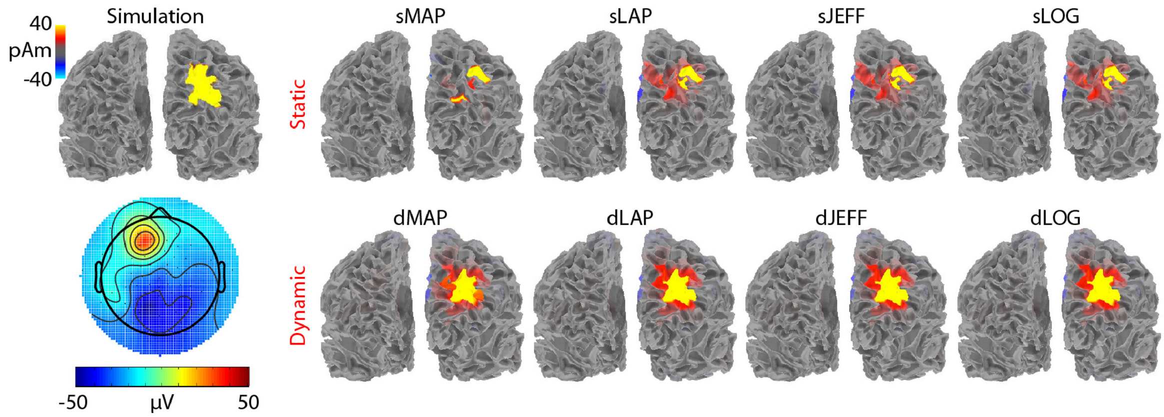


Fig. 4. Left: The top panel shows the extent of the simulated activity at a representative point in time. The bottom panel shows the topographical map of the electrical potentials at the same time instant. Right: Results for the simulated data, shown in the upper row for the static models (sMAP(1st column), sLAP (2nd column), sJEFF (3rd column), and sLOG (4th column)), and shown in the bottom row for the dynamic state-space models (dMAP (1st column), dLAP (2nd column), dJEFF (3rd column), and dLOG (4th column)). The color-bar units for the cortical maps are pAm, whereas for the topographical map of the EEG sensors are $\mu$ V. The color-bar maximum (bright yellow) and minimum (bright blue) for the cortical maps were fixed at +/- twice the standard deviation of the distribution for the estimated currents (i.e., top $5\%$ of the estimates) for both the static and dynamic models. The estimated cortical currents were thresholded at +/- 1 standard deviation [12] and [31]. We found that the dynamic estimates had spatial distributions that corresponded more closely to the true active region compared to static estimates, particularly when sparse prior models were used.

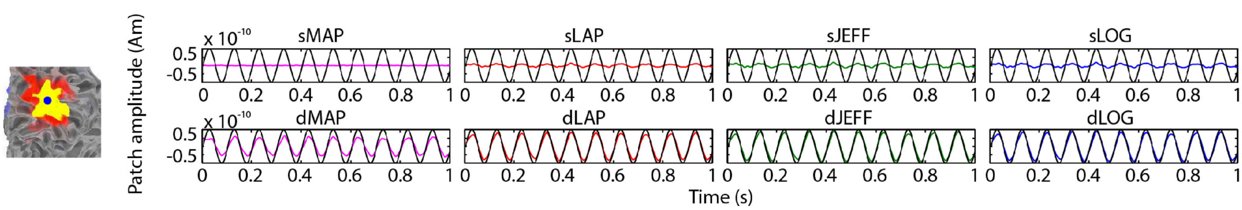


Fig. 5. Time courses estimates for a representative patch inside the true active region. The patch is denoted by a blue dot in the left panel. The static models are shown in the top panels (sMAP (magenta line), sLAP (red line), sJEFF (green line), and sLOG (blue line)), and the dynamic models are shown in the bottom panels (dMAP(magenta line), dLAP (red line), dJEFF (green line), and dLOG (blue line)). The simulated signals are shown in black. The dynamic models, particularly when sparse priors and an empirically-tailored basis are used (dLAP, dJEFF, dLOG), gave the best tracking of the time course of the simulated activity.

## D. Results: Experimental Data

To illustrate the performance of our proposed algorithms on an experimental EEG data, we estimated the sources of spontaneous alpha oscillations (8–12 Hz) elicited during wakeful eyes-closed relaxation. Alpha rhythms are thought to originate in the occipital lobe and are visible when the subjects have their eyes closed, but are not visible when the subjects have their eyes open [48]. We report here source localization analyses of one second in the eyes-open condition and one second during the eyes-closed condition selected at random for three human subjects (Figs. 8 and 9). Source localization of spontaneous brain oscillations represent a challenging and highly appropriate testbed for our approach, since in this scenario, the background noise and the neurophysiological signal occur simultaneously, and cannot be estimated separately simply by selecting non-overlapping time intervals.

For all three subjects, the dynamic models appeared to perform better than static models. Compared to static models, the alpha waves localized by the dynamic models were more compact spatially, and covered a larger area of the occipital pole. The static models tended to have highly focal estimates, with source amplitudes that were 10-fold smaller than those obtained using dynamic models, consistent with the signal loss observed in the analysis of simulated data. Among the dynamic models,

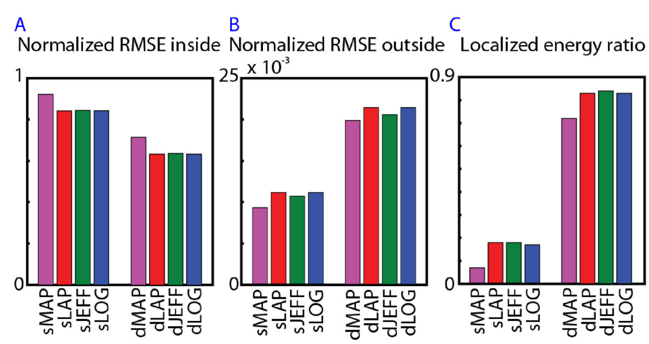


Fig. 6. (a) Average normalized RMSE inside and (b) outside the simulated active region for the different prior models (units pAm). Dynamic state-space models with sparse priors and an empirically-tailored basis (dLAP, dJEFF, dLOG) achieved the lowest value of average RMSE inside the active region. (c) Localized energy ratio for the different prior models. Dynamic state-space models with sparse priors and an empirically-tailored basis (dLAP, dJEFF, dLOG) achieved the highest value of localized energy ratio.

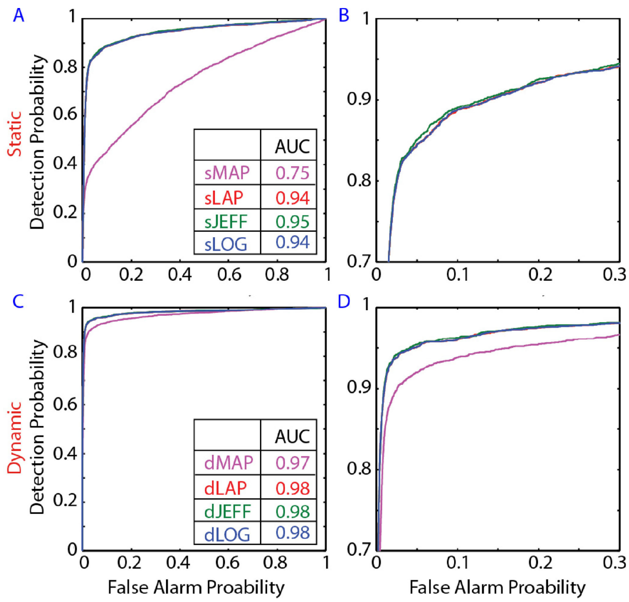


Fig. 7. ROC curves and area under the ROC curves for static models (upper line, Panels A and B) and for dynamic models (bottom line, Panels C and D). Panels B and D provide a zoomed-in view of the left corner of the ROC with detection probability between 0.7-1 and false alarm probability between 0-0.3. The algorithms with an empirically-tailored basis and sparse priors outperformed sMAP and dMAP, detecting more active patches with significantly fewer false alarms. Dynamic state-space models had AUC values that were higher than those of the static models. The use of an empirically-tailored basis and sparse priors in static models made it possible to achieve AUC values similar to those obtained using dynamic models.

TABLE III
COMPUTATIONAL TIME (MEAN +/- STD. DEV. OVER 25 REALIZATIONS) FOR THE THREE DYNAMIC MODELS WITH SPARSE PRIORS AND AN EMPIRICALLY-TAILORED BASIS (DLAP, DJEFF, DLOG)

| Algorithm / Time (min) | dLAP | dJEFF | dLOG |
|---|---|---|---|
| SS-KF and SS-FIS | 10.70 ± 0.08 | 10.83 ± 0.07 | 10.72 ± 0.04 |

The three methods had similar computational performance.

the dMAP estimates appeared to be more focal and spatially irregular compared to the dynamic models utilizing sparse priors and an empirically-tailored basis (dLAP, dJEFF, dLOG). For all the algorithms, the patches that were active during the eyes-closed condition showed substantially lower source amplitudes with eyes open, consistent with what is known about alpha oscillations.

## IV. DISCUSSION

EEG/MEG source localization methods express constraints on the spatial distribution and/or temporal evolution of the underlying source currents of interest [1]–[10]. When viewed in a probabilistic sense, these constraints can be specified in terms of prior distributions [11], [13]–[20], and in particular, in terms of the spatial and/or temporal covariance structure of the sources. In this paper we used a linear dynamical system to specify spatio-temporal constraints for how sources could evolve in time, and introduced novel procedures for sparse, computationally-efficient estimation of the spatial covariance structure of this dynamical system. In addition, we introduced a method for estimating measurement noise within this dynamic system, a component of the system that is both important, and difficult to estimate in EEG studies.

We modeled the spatial covariance structure of the sources using a set of local covariance elements encompassing first- and second-order neighbors (Fig. 1). We then imposed sparse prior models on these covariance components, and used an EM algorithm to estimate them. We found that our new sparse methods improved estimation of the underlying source distributions and time courses (Fig. 6) compared to algorithms that did not employ spatial continuity nor sparsity [12]. We also found that the improvement in performance did not depend upon the form of the sparse prior, and occurred under both static and dynamic models. Previous work by Friston *et al.* [11] described the use of sparse covariance structures for EEG source localization, using model selection procedures to identify the covariance components to include in the model. Our work expresses a similar idea, but formally specifies prior distributions on the covariance elements to promote sparsity. We developed analytical expressions for EM algorithms for the maximum a posteriori estimates of these covariance elements under three different prior distributions. In addition, we applied this sparse covariance structure under both static and dynamic models.

Knowledge of the characteristics of the observation noise is a crucial requirement for source localization algorithms. In MEG recordings the observation noise can be estimated using empty room recordings [36]. However, the situation is more challenging for EEG recordings, since the measurement noise is a function of the skin-electrode interface, necessitating a connection with the subject or patient being studied. In addition, the observation noise in EEG can be interpreted differently depending on the EEG experiment being conducted, e.g., recordings of resting state or spontaneous oscillations, versus evoked-potentials studies. For evoked potential analysis the EEG observation noise can be defined as the activity unrelated to the experiment and thus can be estimated from the pre-stimulus baseline signal [37]. However, in the case of resting-state or spontaneous oscillations, the background observation noise cannot be temporally separated from the overlying neurophysiological signal. In our approach, we overcome this limitation using the EM algorithm to simultaneously estimate the state and observation noise covariances. We employed a number of techniques to make this procedure feasible. We used a multivariate inverse Wishart prior [39] on the observation covariance matrix, and introduced a practical procedure for obtaining initial estimates of the observation covariance using the high-frequency components of the observed signals that would have relatively small physiological signal power.

We also addressed one of the main drawbacks of spatio-temporal dynamic algorithms: the high computational cost [31]. The Kalman Filter (KF) and Fixed-Interval Smoother (FIS) become more computationally demanding as the dimension of the state space increases. This is because, at each step in time, for both the KF and FIS, the expressions for the state covariance matrix, required for state estimation, involve multiplication and

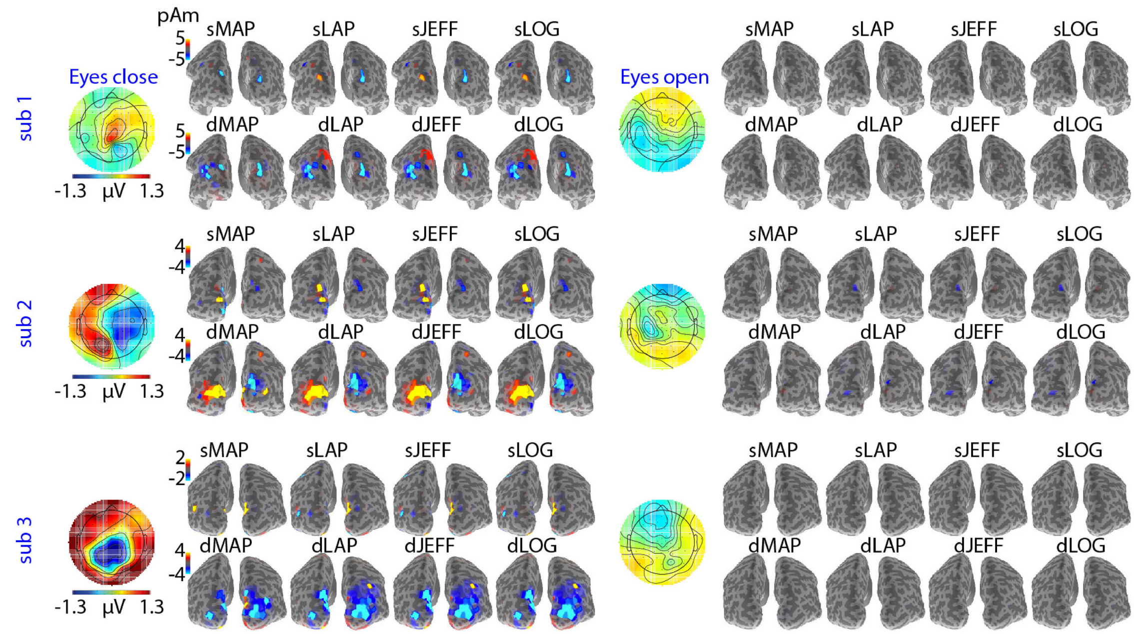


Fig. 8. Analysis of human EEG alpha rhythms for three healthy subjects for over one second in the eyes-open and eyes-closed conditions. The color-bar units for the cortical maps are pAm. The color-bar maximum (bright yellow) and minimum (bright blue) for the cortical maps were fixed at +/- twice the standard deviation of the distribution for the estimated currents for both the static and dynamic models (i.e., top $5\%$ of the estimates) [12] and [31]. The estimated cortical currents were thresholded at +/- 1 standard deviation. The maximum, minimum, and middle values were fixed for each subject separately. The same maximum, minimum, and middle values were used for the eyes-open condition. The maps show the spatial distribution of the estimated activity in the alpha band (8-12 Hz) at a time point corresponding to the maximum of the localized sources. For each subject we also reported the scalp topography of the electric potential during the eyes-open and eyes-closed conditions. The color-bar units for the topographic maps of the EEG sensors are $\mu$ V. The same maximum and minimum values were used for the eyes-open and eyes-closed conditions. Dynamic models with sparse priors and an empirically-tailored basis (dLAP, dJEFF, dLOG) produced estimates of alpha activity in the eyes closed condition that were more compact spatially, covering a larger area of the occipital pole than other methods.

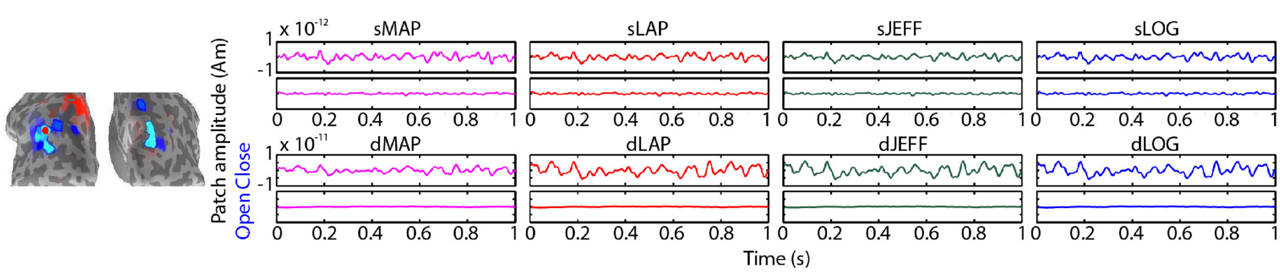


Fig. 9. Time courses of source estimates from experimental data in one subject (the upper subject in Fig. 8). The estimated time series from a representative patch in the right hemisphere (red dot in the left panel), shown in the eyes closed (first line for each method) and eyes open conditions (second line for each method). The results for the different algorithms are organized as above, with the static models in the upper row (sMAP (magenta lines), sLAP (red lines), sJEFF (green lines), and sLOG (blue lines)), and the dynamic models in the bottom row (dMAP (magenta lines), dLAP (red lines), dJEFF (green lines), and dLOG (blue lines)). Note that the results for the static model are shown in units that are 10-fold smaller than the dynamic models, reflecting the same significant reductions in signal amplitude under static models shown earlier in the analysis of simulated data. All methods produced time series consistent with the physiology of alpha waves, showing higher-amplitude oscillations during the eyes closed condition and smaller amplitudes with eyes open.

inversion of large matrices whose dimensions are governed by the size of the state space. Moreover, these matrices must be stored at each point in time. In the case of EEG/MEG source localization under a distributed source model, the state space can encompass 1000's of sources. These complexities and costs are compounded within the EM algorithm, which requires multiple iterations of the KF and FIS. In this paper, we introduced steady-state versions of Kalman Filter (SS-KF) and Fixed Interval Smoother (SS-FIS), replacing the state covariance computation at each time step with a steady state approximation that is computed only once. In a state space model with $N_x$ states and $N_y$ observations, where $N_x > N_y$, the complexity for a single recursion of the KF is $O(N_x^3)$. For the steady state version, this complexity is reduced to $O(N_x)$ [45]. In practice, we found that the SS-KF and SS-FIS reduced the computational time by more than 12-fold compared to the full KF/FIS method, with negligible loss of estimation accuracy (Fig. 2). This significant improvement in computational time would allow these algorithms to be applied more widely in neuroscience or clinical applications, particularly when large amounts of data must be analyzed, as in studies of sleep, epilepsy, or resting state oscillations. The computational cost is also dependent on the complexity of the forward model. However, the computational requirements for realistic boundary element method (BEM) models, which achieve a practical compromise between accuracy of the solution and computational efficiency [49], are negligible compared to those for the inverse solutions discussed in this paper.

We demonstrated the performance of our algorithm on both simulated and experimental high-density EEG recordings. We focused our analysis on spontaneous oscillations, which are important in many neuroscience and clinical applications, including studies of anesthesia [50]–[53], sleep [50], epilepsy [54], and resting state functional networks [55]–[59]. Our results were consistent across both scenarios (i.e., experimental and simulated data). The dynamic models tended to recover distributed source activity better than the static models, most likely due to the local interactions contained in the dynamic models. Moreover, the static models tended to drastically under-estimate the amplitude of source currents, by a factor of ∼10-fold. By contrast, the dynamic models recovered significantly higher amplitude sources, closely matching the true source amplitudes in the simulated data.

In this work, we focused on estimating the source and observation noise covariances. Other parameters, such as those that govern the correlations between dipoles in the source covariance matrix (i.e., $\delta_1$, and $\delta_2$), and the interactions between dipoles in the transition matrix $F$ (i.e., , $a_i$), were selected *a priori* as a practical matter to limit the complexity of the algorithm. We performed additional simulation studies using different choices for these parameters (see Supplementary Material Section IV), and found that the performance remained comparable, suggesting that the method can perform well under a variety of circumstances.

The transition matrix $F$ also plays a role in the tracking performance of our algorithms. When using Bayesian filters (e.g. the Kalman Filter), the key factor in determining the trackability is the set of eigenvalues of the matrix $(I - KG)F$, where $K$ is the steady-state Kalman gain [60], [61]. Let $\lambda_{\max} < 1$ be the maximum eigenvalue of this matrix. Then, it can be shown that for an abrupt change of size $\delta$, the filter tracks the change exponentially fast with a rate of $\lambda_{\max}$ but with an offset error of the order of $\frac{\delta}{1-\lambda_{\max}}$ [60]. Thus, the filter will incur a delay of the order $\frac{1}{\log\left(\frac{1}{\lambda_{\max}}\right)}$ samples in detecting abrupt changes. As a result, when $\lambda_{\max}$ is small, the filter has better trackability, which comes with the cost of increasing the estimation variance [61]. In our approach, we construct the transition matrix $F$ to account for the temporal continuity of each patch at time $t$ with respect to the activity of its nearest neighbors at time $t-1$. Therefore, potentially by changing the structure of the matrix $F$, it is possible to control the value of $\lambda_{\max}$ and thereby enhance the tracking performance. In future work, the methods described here could be extended to estimate the transition matrix $F$ based on the observed data. For instance, Cheung *et al.* [62] describe methods for estimating linear autoregressive dynamics among a small number of regions-of-interest using the EM algorithm; such methods could be readily adapted to estimate the elements of the transition matrix $F$. Doing so using formal estimation procedures, such as the empirical Bayes method we have described here or as in Cheung *et al.* [62], would make it possible to tune the tracking performance based on the observed data, and to estimate the dynamics within and between different sources.

Our work illustrates how spatially-distributed source activity can be estimated alongside an underlying sparse constraint. Sparse, spatially-distributed activity is frequently encountered in many neuroscience and clinical scenarios, including stimulus-evoked and resting-state conditions. In future work, the methods described here could be developed further to include more neurophysiologically-informed models that can account for putative patterns of structural or functional connectivity. Such models could include long-range connections between sources, informed by diffusion tensor imaging or functional MRI [63]. These long-range connections could take the form of prior source covariances, as well as dynamic connections within the state transition matrix, both of which could be estimated from the data using methods such as those described by [62]. Elements of [62] and the present work could be readily combined to characterize sparse dynamic cortical networks from EEG and MEG data.

## V. Conclusion

In this work we proposed a novel method for EEG source localization that brings together 1) a linear state-space dynamic modeling to specify spatio-temporal constraints for how sources can evolve in time, 2) sparsity constraints in the spatial covariance structure of this dynamical system, 3) a method for estimating measurement noise within this dynamic system, and 4) novel computationally-efficient estimation algorithms based on steady-state versions of the Kalman Filter and Fixed Interval Smoother. The results showed that our method outperforms previous dynamic methods in terms of spatial localization accuracy and temporal tracking, as demonstrated by RMSE and ROC measures. Moreover, it improves computational time by more than 12-fold over previous dynamic methods, facilitating practical applications in both neuroscience and medicine.

## Appendix

In this appendix we present the equations of the Kalman Filter (KF) [43] and the Fixed Interval Smoother (FIS) [44] used in the E-step. For each *r*th iteration of the E-step, we initialize the states and the state covariance with $x_{0|0}^{(r)} = 0$ and $P_{0|0}^{(r)} = \Sigma_0^{(r-1)}$, respectively.

In the Kalman Filter, we compute, for $t = 1, 2, \ldots, T$, the predicted states and state covariance as:

$$x_{t|t-1}^{(r)} = F x_{t-1|t-1}^{(r)} \tag{28}$$

$$P_{t|t-1}^{(r)} = F P_{t-1|t-1}^{(r)} F' + Q\left(\theta^{(r-1)}\right) \tag{29}$$

and the filtered states and state covariance as:

$$x_{t|t}^{(r)} = x_{t|t-1}^{(r)} + K_t\left(y_t - G x_{t|t-1}^{(r)}\right) \tag{30}$$

$$P_{t|t}^{(r)} = (I - K_t G) P_{t|t-1}^{(r)} \tag{31}$$

where $K_t$ is the Kalman gain and it corresponds to $K_t = P^{(r)}_{t|t-1} G' \left( G P^{(r)}_{t|t-1} G' + C^{(r)} \right)^{-1}$.

In the case of the steady-state version of KF, we obtain the steady-state predicted state covariance as the solution of the discrete algebraic Riccati equation (DARE) using the MacFarlane-Potter-Fath eigen-structure method (See [45] and [46] for details). Then, from the steady-state predicted state covariance, we compute steady-state filtered state covariance and Kalman gain as indicated in Section II-D.

In the Fixed Interval Smoother, we compute, for $t = T - 1, \ldots, 0$, the smoothed states and state covariance:

$$x^{(r)}_{t|T} = x^{(r)}_{t|t} + J_t \left( x^{(r)}_{t+1|T} - x^{(r)}_{t+1|t} \right) \tag{32}$$

$$P^{(r)}_{t|T} = P^{(r)}_{t|t} + J_t \left( P^{(r)}_{t+1|T} - P^{(r)}_{t+1|t} \right) J'_t \tag{33}$$

where $J_t = P^{(r)}_{t|t} F' P^{(r)-1}_{t+1|t}$ is the Smoother gain. We reported the equations for the steady-state smoothed states and state covariance in Section II-D. We use the smoothed states obtained on the last iteration of the EM-algorithm for source localization.

## References


[1] M. S. Hämäläinen and R. J. Ilmoniemi, "Interpreting magnetic fields of the brain: Minimum norm estimates," *Med. Biol. Eng. Comput.*, vol. 32, no. 1, pp. 35–42, 1994.

[2] R. D. Pascual-Marqui *et al.*, "Low resolution electromagnetic tomography: A new method for localizing electrical activity in the brain," *Int. J. Psychophysiol.*, vol. 18, no. 1, pp. 49–65, 1994.

[3] I. F. Gorodnitsky *et al.*, "Neuromagnetic source imaging with FOCUSS: A recursive weighted minimum norm algorithm," *Electroencephalogr. Clin. Neurophysiol.*, vol. 95, no. 4, pp. 231–251, 1995.

[4] B. D. Van Veen *et al.*, "Localization of brain electrical activity via linearly constrained minimum variance spatial filtering," *IEEE Trans. Biomed. Eng.*, vol. 44, no. 9, pp. 867–880, Sep. 1997.

[5] K. Uutela *et al.*, "Global optimization in the localization of neuromagnetic sources," *IEEE Trans. Biomed. Eng.*, vol. 45, no. 6, pp. 716–723, Jun. 1998.

[6] M.-A. Sato *et al.*, "Hierarchical Bayesian estimation for MEG inverse problem," *Neuroimage*, vol. 23, no. 3, pp. 806–826, 2004.

[7] C. Phillips *et al.*, "An empirical Bayesian solution to the source reconstruction problem in EEG," *Neuroimage*, vol. 24, no. 4, pp. 997–1011, 2005.

[8] J. Mattout *et al.*, "MEG source localization under multiple constraints: An extended Bayesian framework," *Neuroimage*, vol. 30, no. 3, pp. 753–767, 2006.

[9] A. Nummenmaa *et al.*, "Hierarchical Bayesian estimates of distributed MEG sources: Theoretical aspects and comparison of variational and MCMC methods," *Neuroimage*, vol. 35, no. 2, pp. 669–685, 2007.

[10] D. P. Wipf and S. S. Nagarajan, "A unified Bayesian framework for MEG/EEG source imaging," *Neuroimage*, vol. 44, no. 3, pp. 947–966, 2009.

[11] K. J. Friston *et al.*, "Multiple sparse priors for the M/EEG inverse problem," *Neuroimage*, vol. 39, no. 3, pp. 1104–1120, 2008.

[12] C. Lamus *et al.*, "A spatiotemporal dynamic distributed solution to the MEG inverse problem," *Neuroimage*, vol. 63, no. 2, pp. 894–909, 2012.

[13] S. Baillet and L. Garnero, "A Bayesian approach to introducing anatomo-functional priors in the EEG/MEG inverse problem," *IEEE Trans. Biomed. Eng.*, vol. 44, no. 5, pp. 374–385, May 1997.

[14] A. Bolstad *et al.*, "Space-time event sparse penalization for magneto-/electroencephalography," *Neuroimage*, vol. 46, no. 4, pp. 1066–1081, 2009.

[15] J. Daunizeau *et al.*, "Bayesian spatio-temporal approach for EEG source reconstruction: Conciliating ECD and distributed models," *IEEE Trans. Biomed. Eng.*, vol. 53, no. 3, pp. 503–516, Mar. 2006.

[16] J. Daunizeau and K. J. Friston, "A mesostate-space model for EEG and MEG," *Neuroimage*, vol. 38, no. 1, pp. 67–81, 2007.

[17] F. Greensite, "The temporal prior in bioelectromagnetic source imaging problems," *IEEE Trans. Biomed. Eng.*, vol. 50, no. 10, pp. 1152–1159, Oct. 2003.

[18] T. Limpiti *et al.*, "A spatiotemporal framework for estimating trial-to-trial amplitude variation in event-related MEG/EEG," *IEEE Trans. Biomed. Eng.*, vol. 56, no. 3, pp. 633–645, Mar. 2009.

[19] N. J. Trujillo-Barreto *et al.*, "Bayesian M/EEG source reconstruction with spatio-temporal priors," *Neuroimage*, vol. 39, no. 1, pp. 318–335, 2008.

[20] J. M. Zumer *et al.*, "Probabilistic algorithms for MEG/EEG source reconstruction using temporal basis functions learned from data," *Neuroimage*, vol. 41, no. 3, pp. 924–940, 2008.

[21] A. Galka *et al.*, "A solution to the dynamical inverse problem of EEG generation using spatiotemporal Kalman filtering," *Neuroimage*, vol. 23, no. 2, pp. 435–453, 2004.

[22] O. Yamashita *et al.*, "Recursive penalized least squares solution for dynamical inverse problems of EEG generation," *Hum. Brain Mapping*, vol. 21, no. 4, pp. 221–235, 2004.

[23] C. J. Long *et al.*, "State-space solutions to the dynamic magnetoencephalography inverse problem using high performance computing," *Ann. Appl. Statist.*, vol. 5, no. 2B, pp. 1207–1228, 2011.

[24] C. Lamus *et al.*, "Parameter estimation and dynamic source localization for the magnetoencephalography (MEG) inverse problem," in *Proc. 4th IEEE Int. Symp. Biomed. Imag. Nano Macro*, Washington, DC, USA, 2007, pp. 1092–1095.

[25] O. David *et al.*, "Dynamic causal modeling of evoked responses in EEG and MEG," *Neuroimage*, vol. 30, no. 4, pp. 1255–1272, 2006.

[26] W. Ou *et al.*, "A distributed spatio-temporal EEG/MEG inverse solver," *Neuroimage*, vol. 44, no. 3, pp. 932–946, 2009.

[27] A. Gramfort *et al.*, "Functional brain imaging with M/EEG using structured sparsity in time-frequency dictionaries," in *Information Processing in Medical Imaging*. New York, NY, USA: Springer, 2011, pp. 600–611.

[28] A. Gramfort *et al.*, "Mixed-norm estimates for the M/EEG inverse problem using accelerated gradient methods," *Phys. Med. Biol.*, vol. 57, no. 7, pp. 1937–1961, 2012.

[29] T. Tian and Z. Li, "A spatio-temporal solution for the EEG/MEG inverse problem using group penalization methods," *Statist. Interface*, vol. 4, pp. 521–533, 2011.

[30] T. Tian *et al.*, "A two-way regularization method for MEG source reconstruction," *Ann. Appl. Statist.*, vol. 6, no. 3, pp. 1021–1046, 2012.

[31] B. Babadi *et al.*, "A subspace pursuit-based iterative greedy hierarchical solution to the neuromagnetic inverse problem," *Neuroimage*, vol. 87, pp. 427–443, 2014.

[32] W.-T. Chang *et al.*, "Spatially sparse source cluster modeling by compressive neuromagnetic tomography," *Neuroimage*, vol. 53, no. 1, pp. 146–160, 2010.

[33] M. Zhu *et al.*, "Reconstructing spatially extended brain sources via enforcing multiple transform sparseness," *Neuroimage*, vol. 86, pp. 280–293, 2014.

[34] A. Sohrabpour *et al.*, "Imaging brain source extent from EEG/MEG by means of an iteratively reweighted edge sparsity minimization (IRES) strategy," *Neuroimage*, vol. 142, pp. 27–42, 2016.

[35] K. Liu *et al.*, "Bayesian electromagnetic spatio-temporal imaging of extended sources with Markov random field and temporal basis expansion," *Neuroimage*, vol. 139, pp. 385–404, 2016.

[36] M. Hämäläinen *et al.*, "Magnetoencephalography—Theory, instrumentation, and applications to noninvasive studies of the working human brain," *Rev. Mod. Phys.*, vol. 65, no. 2, pp. 413–497, 1993.

[37] S. Baillet *et al.*, "Electromagnetic brain mapping," *IEEE Signal Process. Mag.*, vol. 18, no. 6, pp. 14–30, Nov. 2001.

[38] E. Pirondini *et al.*, "A spatially-regularized dynamic source localization algorithm for EEG," in *Proc. 2012 Annu. Int. Conf. IEEE Eng. Med. Biol. Soc.*, 2012, pp. 6752–6755.

[39] A. Gelman *et al.*, *Bayesian Data Analysis*. Boca Raton, FL, USA: CRC, 2003.

[40] B. Fischl *et al.*, "Cortical surface-based analysis. II: Inflation, flattening, and a surface-based coordinate system," *Neuroimage*, vol. 9, no. 2, pp. 195–207, 1999.

[41] M. Figueiredo, "Adaptive sparseness using jeffreys prior," in *Proc. Adv. NIPS*, 2001, pp. 697–704.

[42] A. Bruckstein *et al.*, "From sparse solutions of systems of equations to sparse modeling of signals and images," *SIAM Rev.*, vol. 51, no. 1, pp. 34–81, 2009.

[43] R. Kalman, "A new approach to linear filtering and prediction problems," *J. Basic Eng.*, vol. 82, no. 1, pp. 35–45, 1960.

[44] H. Rauch *et al.*, "Maximum likelihood estimates of linear dynamic systems," *AIAA J.*, vol. 3, no. 8, pp. 1445–1450, 1965.

[45] W. Malik *et al.*, "Efficient decoding with steady-state Kalman filter in neural interface systems," *IEEE Trans. Neural Syst. Rehabil. Eng.*, vol. 19, no. 1, pp. 25–34, Feb. 2011.

[46] C. Chui and G. Chen, *Kalman Filtering: With Real-Time Applications*. New York, NY, USA: Springer, 2008.

[47] T. Limpiti *et al.*, "Cortical patch basis model for spatially extended neural activity," *IEEE Trans. Biomed. Eng.*, vol. 53, no. 9, pp. 1740–1754, Sep. 2006.

[48] W. Freeman *et al.*, "Combining fMRI with EEG and MEG in order to relate patterns of brain activity to cognition," *Int. J. Psychophysiol.*, vol. 73, no. 1, pp. 43–52, 2009.

[49] K. Wendel *et al.*, "EEG/MEG source imaging: Methods, challenges, and open issues," *Comput. Intell. Neurosci.*, vol. 2009, 2009, Art. no. 13.

[50] M. Murphy *et al.*, "Propofol anesthesia and sleep: A high-density EEG study," *Sleep*, vol. 34, no. 3, pp. 283–291, 2011.

[51] E. A. Mukamel *et al.*, "A transition in brain state during propofol-induced unconsciousness," *J. Neurosci.*, vol. 34, no. 3, pp. 839–845, 2014.

[52] R. N. Mhuircheartaigh *et al.*, "Slow-wave activity saturation and thalamocortical isolation during propofol anesthesia in humans," *Sci. Transl. Med.*, vol. 5, no. 208, pp. 208ra148–208ra148, 2013.

[53] P. L. Purdon *et al.*, "Electroencephalogram signatures of loss and recovery of consciousness from propofol," *Proc. Nat. Acad. Sci. USA*, vol. 110, no. 12, pp. E1142–E1151, 2013.

[54] F. Amor *et al.*, "Cortical local and long-range synchronization interplay in human absence seizure initiation," *Neuroimage*, vol. 45, no. 3, pp. 950–962, 2009.

[55] H. Yuan *et al.*, "Reconstructing large-scale brain resting-state networks from high-resolution EEG: Spatial and temporal comparisons with fMRI," *Brain Connectivity*, vol. 6, no. 2, pp. 122–135, 2016.

[56] H. Laufs *et al.*, "Where the bold signal goes when alpha EEG leaves," *Neuroimage*, vol. 31, no. 4, pp. 1408–1418, 2006.

[57] H. Laufs *et al.*, "EEG-correlated fMRI of human alpha activity," *Neuroimage*, vol. 19, no. 4, pp. 1463–1476, 2003.

[58] D. Mantini *et al.*, "Electrophysiological signatures of resting state networks in the human brain," *Proc. Nat. Acad. Sci. USA*, vol. 104, no. 32, pp. 13 170–13 175, 2007.

[59] M. G. Kitzbichler *et al.*, "Altered development and multifaceted band-specific abnormalities of resting state networks in autism," *Biol. Psychiatry*, vol. 77, no. 9, pp. 794–804, 2015.

[60] D. Farden, "Tracking properties of adaptive signal processing algorithms," *IEEE Trans. Acoust., Speech, Signal Process.*, vol. 29, no. 3, pp. 439–446, Jun. 1981.

[61] L. Ljung, "General structure of adaptive algorithms: adaptation and tracking," in *Adaptive System Identification and Signal Processing Algorithms*. Englewood Cliffs, NJ, USA: Prentice-Hall, 1993, pp. 58–83.

[62] B. L. P. Cheung *et al.*, "Estimation of cortical connectivity from EEG using state-space models," *IEEE Trans. Biomed. Eng.*, vol. 57, no. 9, pp. 2122–2134, Sep. 2010.

[63] M. Fukushima *et al.*, "MEG source reconstruction based on identification of directed source interactions on whole-brain anatomical networks," *Neuroimage*, vol. 105, pp. 408–427, 2015.